nature materials

ARTICLES

PUBLISHED ONLINE: 23 MAY 2016 | DOI: 10.1038/NMAT4649

Reversible optical switching of highly confined phonon–polaritons with an ultrathin phase-change material

Peining Li, Xiaosheng Yang, Tobias W. W. Maß, Julian Hanss, Martin Lewin, Ann-Katrin U. Michel, Matthias Wuttig and Thomas Taubner*

Surface phonon–polaritons (SPhPs), collective excitations of photons coupled with phonons in polar crystals, enable strong light–matter interaction and numerous infrared nanophotonic applications. However, as the lattice vibrations are determined by the crystal structure, the dynamical control of SPhPs remains challenging. Here, we realize the all-optical, non-volatile, and reversible switching of SPhPs by controlling the structural phase of a phase-change material (PCM) employed as a switchable dielectric environment. We experimentally demonstrate optical switching of an ultrathin PCM film (down to 7 nm, $< \lambda/1{,}200$) with single laser pulses and detect ultra-confined SPhPs (polariton wavevector $k_p > 70k_0, k_0 = 2\pi/\lambda$) in quartz. Our proof of concept allows the preparation of all-dielectric, rewritable SPhP resonators without the need for complex fabrication methods. With optimized materials and parallelized optical addressing we foresee application potential for switchable infrared nanophotonic elements, for example, imaging elements such as superlenses and hyperlenses, as well as reconfigurable metasurfaces and sensors.

Polar crystals, such as silicon carbide (SiC), hexagonal boron nitride (hBN) and quartz, have recently emerged as an exceptional platform for infrared nanophotonics[1–6]. Their permittivities exhibit a negative real part inside their Reststrahlen band—a spectral range between the longitudinal and transverse optical phonons of a polar crystal. Furthermore, the imaginary part of their permittivities can also be small within the Reststrahlen band. The combination of low losses and negative permittivities allows polar crystals to support highly confined surface phonon–polaritons (SPhPs) with a lifetime (~1 ps (ref. 5)) much longer than the surface waves employed as surface plasmon–polaritons (SPPs) in metals. The low losses, along with the strong field confinement and the short wavelength of SPhPs, thus make them a superior alternative to metals and offer the promise of a wide range of optical and thermal applications, such as sub-diffractional resonators[7–9], super-resolution imaging[10–12], waveguiding and focusing[6,11,12], and tailored coherent thermal emission[13].

However, SPhPs on polar crystals still have two disadvantages that could limit their further application prospects. First, for the propagation of SPhPs with ultrashort wavelengths, a very thin layer[2] or wire[14] of a polar crystal is needed. On a three-monolayer hBN flake[2] (thickness <1 nm), the propagation of SPhPs with a wavevector of k_p up to $25k_0$ has been demonstrated[2]. On increasing the flake thickness to 500 nm, the SPhP wavevector decreases to approximately $3k_0$. Thus, SPhPs ($k_p \sim k_0$) on a bulk substrate of a polar crystal provide significant, but not ultimate field confinement compared to the cases of thin layers or wires of polar crystals.

Second, because SPhPs originate from intrinsic lattice vibrations of polar crystals, their active tuning functionalities are limited. This hinders their application for tunable and reconfigurable nanophotonics. Recent works have demonstrated that SPhPs in a graphene–hBN heterostructure can be modified by means of phonon–plasmon–polariton hybridization[15–17]. This hybridization concept can be generalized for the bottom-up creation of new materials with tailorable SPhP dispersion[18], but requires complex fabrication. The tuning of phonon–plasmon hybrids by means of optical or electrical control of the charge carrier density in polar crystals is also possible[19], but remains volatile—that is, the tuning vanishes after the excitation is switched off.

Phase-change materials for active nanophotonics

Phase-change materials (PCMs) could offer a new way to solve those problems simultaneously. PCMs based on chalcogenide alloys have been used in non-volatile, rewritable data storage and memory[20]. They possess two room-temperature stable phases, an amorphous state and a crystalline state, which differ distinctly in their optical and electrical properties. These two phases can be reversibly and rapidly[21] switched by applying either optical or electrical pulses. In particular, by using femtosecond laser pulses, PCMs have also been recently considered as a versatile platform for infrared active nanophotonics with metallic nanostructures owing to their switchable and low-loss dielectric properties[22–28]. For instance, the $Ge_3Sb_2Te_6$ compound (GST-326) shows a large difference in the real part of the permittivity between the amorphous (a-) and the crystalline (c-) phases within a broad mid-infrared wavelength region ($\varepsilon_{a\text{-GST}} \approx 12 + 0i$, $\varepsilon_{c\text{-GST}} \approx 36 + 2.5i$ at least from 800 to 2,500 cm^{-1}), whereas the imaginary part of both phases is comparatively small ($\mathrm{Im}(\varepsilon)/\mathrm{Re}(\varepsilon) < 0.1$)[23,24].

Based on these unique dielectric properties, the low-loss resonance switching of metallic resonant antennas with very high Q-factor has been achieved[23,24]. By choosing different PCMs with advanced properties, such as a high-index crystalline (amorphous) state and a low-index amorphous (crystalline) state, they can select between a red- or a blueshift of the resonance. Femtosecond

Institute of Physics (IA), RWTH Aachen University, Aachen 52056, Germany. *e-mail: taubner@physik.rwth-aachen.de

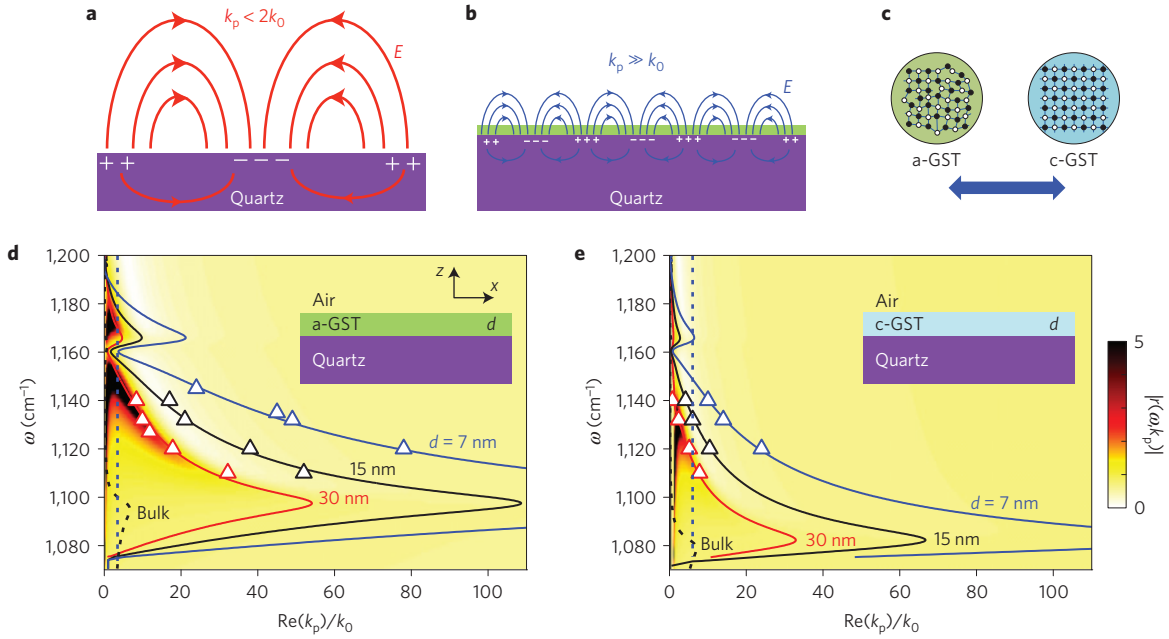

Figure 1 | Ultra-confined SPhPs enabled by an ultrathin GST layer on quartz. a–c, Sketch of our concept: as indicated by the lines of the electric field *E*, a thin layer of GST (**b**) squeezes the wavelength of SPhPs of a bare quartz surface significantly (**a**) and can be reversibly switched between its amorphous (a-GST) and crystalline (c-GST) state (**c**). **d**,**e**, Solid lines are the calculated dispersion relations of slow SPhP modes within a quartz Reststrahlen band (1,070–1,230 cm^{-1}) for amorphous (**d**) and crystalline (**e**) GST films ($d = 7$, 15 and 30 nm) on quartz substrates. Black dashed lines show calculated SPhP dispersion for bulk GST ($d \to \infty$) on quartz. Blue vertical lines indicate the positions of Re(k_p) $= \sqrt{\varepsilon_{a\text{-GST}}}k_0$ and Re(k_p) $= \sqrt{\varepsilon_{c\text{-GST}}}k_0$, respectively. Triangles show the experimentally extracted data from s-SNOM measurements on various samples and structures. False-colour plots show calculated reflection coefficients $|r(\omega,k_p)|$ of the GST(30-nm)/quartz stacks as a function of the frequency ω and the wavevector k_p.

laser pulses have been used to reversibly modulate the resonance of metallic hole structures[27]. This modulation is induced by the femtosecond pulse excitation, which causes a rapid depletion of electrons from resonantly bonded crystalline PCM[28]. The laser power used is far below the threshold required for the permanent phase transition. Hence, the femtosecond pulses enable an ultrafast and reversible change in the dielectric function of the PCM, allowing the ultrafast modulation of the PCM-covered metallic structures. Recently, optically reconfigurable all-PCM-based metasurfaces and photonic devices have been demonstrated[22]. A laser beam with pattern generators has been used to write and erase multiple PCM structures simultaneously for creating flat, rewritable dielectric lenses and resonators. As this work relies on high-index dielectric resonators and does not incorporate any polaritonic materials, it is limited to rather large structures and moderate field confinement.

Ultra-confined SPhPs enabled by a thin PCM film

In this work we combine the local addressing and switching of the PCMs with the strong field confinement of the SPhPs to demonstrate extremely confined SPhPs that can be reversibly controlled by single nanosecond laser pulses. As sketched in Fig. 1a–c, our main idea is to cover a crystalline quartz (as an exemplary polar crystal) substrate with a thin GST film (thickness d), resulting in a strongly modified dispersion of the SPhPs: a bare quartz surface can support SPhPs with only a relatively small wavevector ($k_p < 2k_0$), but the new layer stack can host highly confined SPhPs ($k_p \gg k_0$) with much shorter wavelengths and an additional switching functionality provided by the GST layer.

Similar to SPPs on a thin dielectric layer on a metal[29–31], two SPhP modes also exist in the resulting air/GST/quartz stack: a fast SPhP mode with a relatively high phase velocity and a small wavevector (k_p close to k_0), and a slow SPhP mode with low phase velocity and large wavevector ($k_p \gg k_0$). The dispersion relation of the SPhP modes on the air/GST/quartz stack can be calculated as[31]:

$$\tanh(k_{GST}\varepsilon_{GST}d) = -\frac{k_{air}k_{GST} + k_{GST}k_{quartz}}{k_{GST}^2 + k_{air}k_{quartz}} \quad (1)$$

where $k_i = \sqrt{k_p^2 - \varepsilon_i k_0^2}/\varepsilon_i$, i = air, GST, quartz. ε_i are dielectric permittivities of air, GST and quartz (Supplementary Fig. 1), respectively. In the following we focus on the slow SPhP modes, which provide extreme field confinement. We calculate the dispersion relation of slow SPhP modes within a quartz Reststrahlen band[32] (1,070–1,230 cm^{-1}) for three GST thicknesses ($d = 7$, 15 and 30 nm). The small GST thickness change (~5%, the crystalline phase has a higher density)[33] which occurs during the phase transition is neglected here as is not needed in explaining our main concept. The results are plotted as solid lines in Fig. 1d,e. One can see that SPhPs with high wavevectors exist in two different spectral ranges—for example, 1,070–1,160 cm^{-1} and 1,160–1,190 cm^{-1} for the 30-nm a-GST case. These two ranges are caused by several weak intrinsic phonons of quartz around 1,160 cm^{-1} (Supplementary Fig. 1). For other polar crystals such as SiC, only a major SPhP branch is usually observed (Supplementary Fig. 2).

Apparently, different GST phases lead to large changes of the SPhP dispersion. For the 30-nm thick a-GST, a maximum SPhP wavevector k_p up to $54k_0$ is obtained at 1,097 cm^{-1}. In the c-GST phase, the maximum redshifts to a wavenumber of 1,082 cm^{-1}. However, this redshift causes the SPhP resonances to move into a spectral range where the quartz dielectric function has a larger imaginary part (Supplementary Fig. 1). Therefore, the maximum wavevector k_p for the c-GST case decreases to approximately $33k_0$.

Moreover, decreasing the GST thickness significantly increases the SPhP wavevector k_p—for example, k_p increases to $230k_0$ for the 7-nm a-GST. This exceptional value indicates that, simply by adding a thin GST layer on a polar-crystal substrate, a much larger SPhP

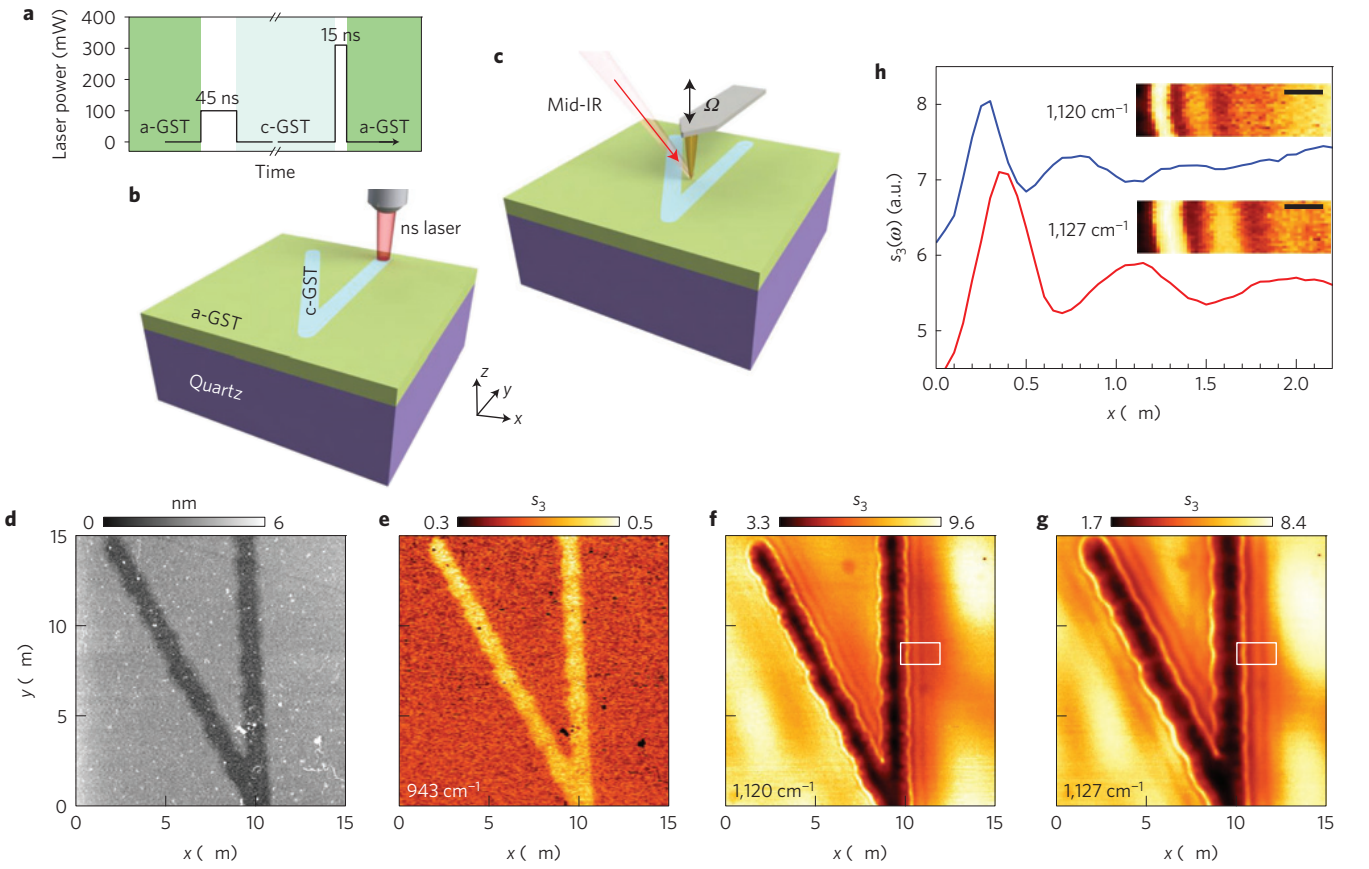

Figure 2 | Real-space imaging of ultra-confined SPhPs. a, Laser parameters used for switching the GST films. **b**, Schematic of switching a V-shaped c-GST domain in a 30-nm-thick a-GST film by scanning a pulsed laser beam with a power of 100 mW and a pulse duration of 45 ns. **c**, Schematic of real-space imaging of SPhPs launched in the V-structure by the s-SNOM. Ω, tip oscillation frequency; IR, infrared. **d**, AFM topographic image. **e**–**g**, s-SNOM images (optical amplitude signals s_3) of the c-GST wedge measured at three different frequencies. At a frequency of 943 cm^{-1} (**e**), outside the quartz Reststrahlen band, no SPhPs are observed because the quartz permittivity is positive at this frequency. Owing to the higher refractive index the c-GST areas are brighter than the surrounding a-GST film. For frequencies inside the quartz Reststrahlen band, 1,120 cm^{-1} (**f**) and 1,127 cm^{-1} (**g**), we observed obvious SPhP fringes due to the negative permittivity of quartz. **h**, Inset images are the details of the areas enclosed in white frames in **f** and **g**. Lines are the corresponding line profiles of s_3, which are averaged over three line scans. Scale bars are 500 nm.

confinement compared to the method of using a thin polar crystal (considering $k_p = 25k_0$ in a 1-nm-thick hBN[2]) can be achieved. We also note that the SPhP confinement can be further improved when replacing the quartz with other polar crystals exhibiting lower damping, such as SiC or hBN. For instance, as calculated in the Supplementary Fig. 2, the wavevector k_p can be increased to $470k_0$ for a 7-nm GST on a SiC substrate.

Switching and imaging of surface phonon–polaritons

To optically switch the GST, single nanosecond laser pulses (centre wavelength: 660 nm) are employed with the parameters depicted in Fig. 2a. Our approach of using a focused nanosecond laser beam is capable of locally switching micrometre-sized domains in the film. Thus it offers great flexibility for local structuring and could in principle be used to rapidly produce even more complex metasurface structures. For the present work, a V-shaped structure consisting of two connected c-GST stripes was switched (Fig. 2b) by scanning single laser pulses (45 ns, 100 mW) in an as-deposited a-GST film ($d \sim 30$ nm). We used a scattering-type scanning near-field microscope[1,2,6] (s-SNOM) to characterize the SPhPs excited in this structure, which is a tapping-mode atomic force microscope (AFM) coupled with mid-infrared laser sources (Fig. 2c). The sharp s-SNOM tip acting as an optical antenna can provide the missing momentum to launch the SPhPs[2,6]. In addition, the a-/c-GST boundary can also generate (Supplementary Fig. 3) and reflect the SPhPs, forming standing-wave interference fringes that can be visualized by the s-SNOM[2,6].

Figure 2d shows the AFM topography, in which the switched c-GST area appears 1.5 nm lower than the a-GST film owing to an increase in film density by the crystallization[33]. The optical images recorded by s-SNOM are shown in Fig. 2e–g. At a frequency of 943 cm^{-1} (Fig. 2e), the high-index c-GST areas are brighter than the surrounding a-GST film. No SPhPs are found because the quartz permittivity is positive at this frequency. When tuning the laser frequency inside the quartz Reststrahlen band (Fig. 2f,g), we observed obvious SPhP fringes due to the negative permittivity of quartz.

To extract the polariton wavevector k_p from measured fringes (zoom in, Fig. 2h), we used a standing-wave model containing three SPhP terms (Supplementary Note 1): boundary-launched SPhPs, tip-launched SPhPs, tip-launched and boundary-reflected SPhPs. This model revealed that the measured fringe period is almost equal to the SPhP wavelength λ_p (Supplementary Fig. 4). The extracted k_p (see coloured triangles in Fig. 1d,e) is in good agreement with theoretical calculations, for example, the experimental value $\mathrm{Re}(k_p) = 17.9k_0$ ($\lambda_p \approx 500$ nm) and the theoretical value of $\mathrm{Re}(k_p) = 17.8k_0$ at 1,120 cm^{-1} agree very well. For the 7-nm a-GST, we observed k_p values up to $74k_0$ (Supplementary Fig. 5), which is three times higher than previously reported[2], but below the highest wavevectors predicted by the dispersion calculations (equation (1)).

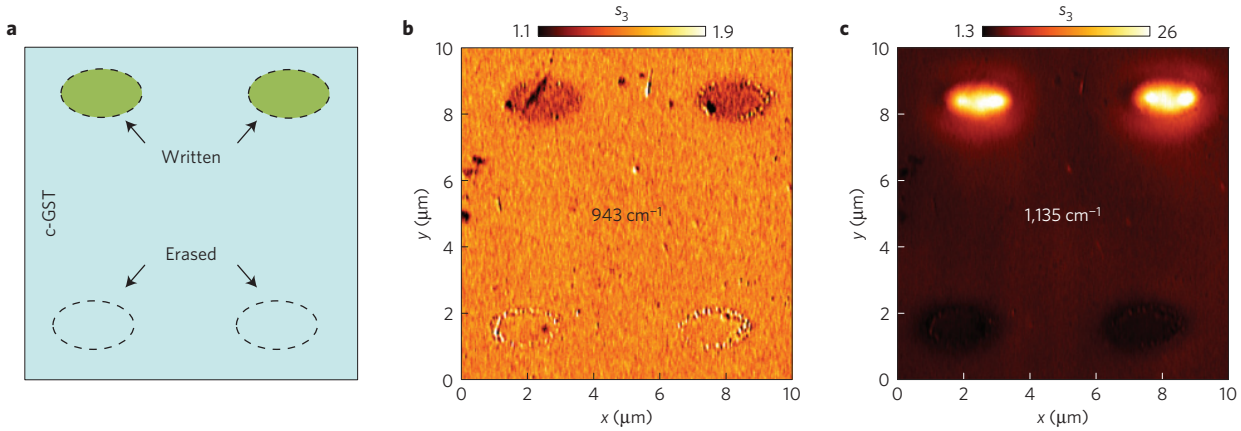

Figure 3 | s-SNOM imaging of reversibly switched GST SPhP resonators. a, Schematic, top view of single elliptical a-GST domains written (amorphized) in a thermally transformed c-GST film (around 30-nm thick) by 15 ns laser pulses with a power of 310 mW. The lower two domains were erased (recrystallized) by 45 ns laser pulses with a power of 100 mW. **b**,**c**, Optical images (s_3) of these four domains taken at a frequency outside the Reststrahlen band (no SPhPs) 943 cm^{-1} (**b**) and inside the Reststrahlen band (with SPhP excitation) 1,135 cm^{-1} (**c**).

The reason for this difference is that these calculations give only the theoretical wavevector values, but do not reveal the strength of the reflected SPhP fields. The detected s-SNOM signals, however, are related to the strength of the reflected fields[1,2]. For a proper comparison, we also show the calculated reflection coefficient $|r(\omega, k_p)|$ of the 30-nm-GST/quartz stack (other thicknesses in Supplementary Figs 6 and 7) as a function of frequency ω and wavevector k_p as false-colour plots in Fig. 1d,e. The reflection peaks (indicated by dark colours) in the maps originate from the SPhP modes, and their colour indicates the corresponding SPhP field strength. Their reflection field strength decays with increasing k_p, owing to stronger field confinement in the layer. This decay causes the limited observation of k_p in our s-SNOM experiments. Moreover, the lower branches of SPhPs modes (for example, $1{,}072 < \omega < 1{,}097$ cm^{-1} for 30-nm a-GST) cannot be revealed in the maps of $|r(\omega, k_p)|$ or the s-SNOM measurements. They are the so-called quasi-bound polariton modes[34], which have a large absorption and decay fast in the layers.

Reversible optical switching of SPhP/PCM resonators

The laser-induced local switching of the GST promises a large variety of new SPhP applications. As a first example, we present all-dielectric rewritable SPhP resonators that are switched in the GST film on quartz. As sketched in Fig. 3a, four elliptical a-GST domains (major axis $a \sim 1.8$ μm, minor axis $b \sim 1$ μm, also see Supplementary Fig. 8) were 'written' in a 30-nm thermally initialized c-GST film by applying single laser pulses (15 ns, 310 mW). Subsequently, 45 ns laser pulses with a power of 100 mW were employed to 'erase' (recrystallize) the lower two domains. The switched sample area was characterized by our s-SNOM. At a frequency of 943 cm^{-1} (Fig. 3b), the upper two a-GST domains are darker than the surrounding c-GST film. The lower two (erased) areas show almost no contrast, as expected, validating a successful erasure (recrystallization) process. At a frequency of 1,135 cm^{-1}, located inside the Reststrahlen band (Fig. 3c), strong SPhP fields are observed within laser-written a-GST domains (more data in Supplementary Fig. 9). This is because the a-/c-GST interfaces formed act as reflecting boundaries for the SPhPs, giving rise to a dielectric SPhP cavity resonator.

To clearly reveal the resonances of those elliptical cavity resonators, we simulated and measured far-field reflection spectra. Figure 4a plots simulated far-field reflection spectra of an array of a-GST resonators ($a = 1.7$ μm, $b = 0.9$ μm) in a c-GST film (30-nm thick). The dip around 1,130 cm^{-1} in the spectrum corresponds to the SPhP cavity resonances, as it shows a clear dependence on the electric-field polarization expected from the elliptical shape of the resonators. Namely, its resonance position is blueshifted when changing the polarization from the *E*-long direction (parallel to the major axis of the resonator) to the *E*-short direction (parallel to the minor axis). Here the SPhP resonators show a reflection dip at resonance, in contrast to plasmonic resonators usually exhibiting a reflection peak. SPhP resonances are superimposed on the highly reflective Reststrahlen band of the polar crystal, thus showing as absorption features in the reflection spectra[7,8]. The polarization-independent peak in the spectrum at around 1,160 cm^{-1} is due to intrinsic quartz phonons. We also note that the modal behaviour of our SPhP resonators is similar to elliptical plasmonic nanoantennas[35]. They are due to the constructive interference of SPhPs launched and reflected at the laser-switched a-GST/c-GST boundaries. Our simulated field distributions (the insets in Fig. 4a) verify that for the *E*-short direction the resonance is the fundamental (1,1) mode and for the *E*-long direction it is a higher order (1,2) mode. Further information on the modal behaviour in elliptical resonators is provided in Supplementary Note 2. Interestingly, we also observe a resonance in the opposite configuration of a c-GST spot switched in the a-GST film (Supplementary Fig. 10), where the working mechanism of the resonators is similar to conventional metallic hole resonators.

Experimental far-field spectra of an array of elliptical resonators (4×4 a-GST resonators in an area of about 20×20 μm^2) written in the 30-nm-thick c-GST film are shown in Fig. 4b,c. The SPhP cavity resonances depend on the polarization, as expected. They are at 1,130 cm^{-1} for the *E*-long direction and at 1,136 cm^{-1} for the *E*-short direction. These sharp resonances have *Q*-factors ($=\omega_0$/FWHM, full-width at half-maximum) up to 95, larger than that of the metallic hole-cavity SPhP resonance[8] ($Q < 75$), presumably because the low-loss all-dielectric constituents avoid potential losses, as found in metals. These high-*Q*-factor resonators could be used for mid-IR sensing and enhanced spectroscopy[36,37], as well as optical switches and modulators. For those applications, the SPhP resonances of our structures can be enhanced in different ways, such as using polar crystals with lower losses (Supplementary Fig. 11), optimizing the array parameters (Supplementary Fig. 12), or designing more efficient structures (Supplementary Fig. 13).

The same resonator structures were also investigated for even thinner GST thicknesses (7 and 15 nm). However, the resonances of those thinner resonators are much less pronounced compared to the 30-nm-thick cases. We attribute this to the stronger localization and shorter wavelength of the SPhPs in those thinner layers, which would require smaller cavities to efficiently excite the resonance.

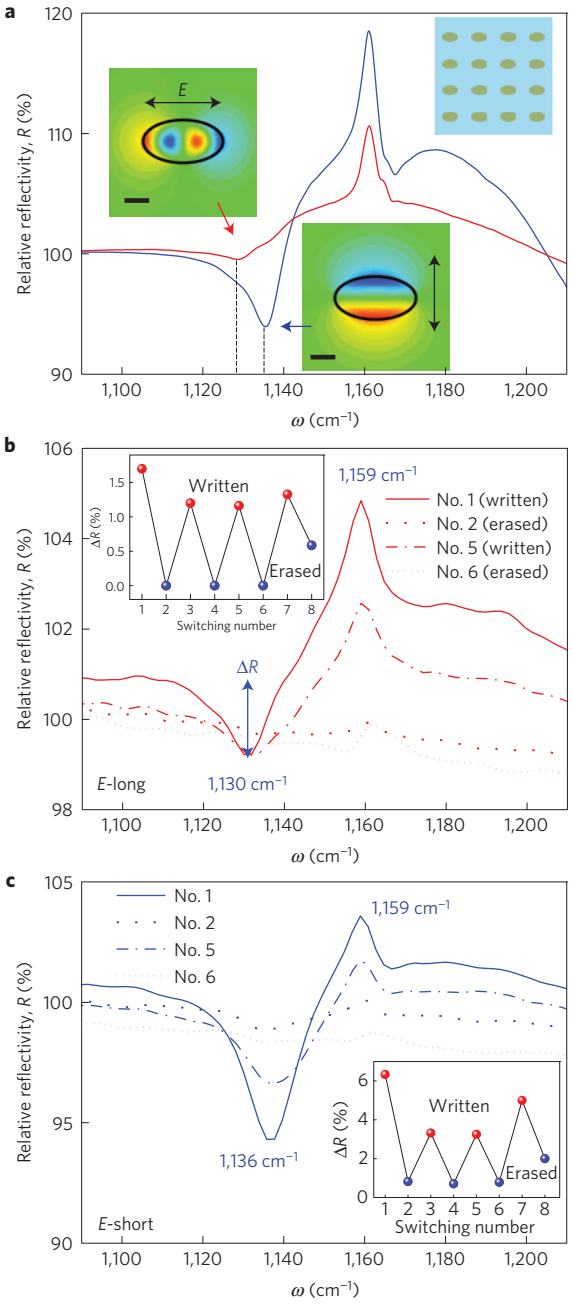

Figure 4 | Far-field reflection of rewritable SPhP resonators. **a**, Simulated reflection spectra of an array (sketched in the top right inset) of a-GST SPhP resonators (major axis $a = 1.7\,\mu m$, minor axis $b = 0.9\,\mu m$) in a c-GST film (30 nm) on quartz for two polarizations. They are normalized to the calculated reflectance of a flat 30-nm c-GST film on quartz. The colour insets show the electric-field ($Re(E_z)$) distribution at two resonances of these SPhP resonators. The double-headed arrow indicates the direction of polarization. Scale bars are 500 nm. **b**,**c**, Measured far-field reflection spectra for polarizations in the *E*-long direction (parallel to the major axis of the resonator) (**b**) and the *E*-short direction (parallel to the minor axis) (**c**). All the reflection spectra are normalized to the surrounding c-GST film with the same detection size. These resonators were reversibly switched multiple times. The insets show the variation of the amplitude of ΔR (indicated by a blue arrow in **b**) of the resonances with the switching times.

Most importantly, by applying an erasure pulse, the spectral features of the SPhP resonance were removed, as can be seen from the measured spectra (dashed lines in Fig. 4b,c). We also performed multiple-time rewritable experiments. The multiple-time switching suppressed both the *Q*-factor and the resonance strength (indicated by ΔR). The number of switching events in these initial experiments is found to be limited to 8 (the insets in Fig. 4b,c and Supplementary Fig. 14), which might be caused by laser-induced film ablation (Supplementary Fig. 8). The main reason for this limitation is the absence of a protective capping layer for better s-SNOM visualization of the SPhPs. We note that the number of switching events can easily be improved by adding a protective layer of ZnS:SiO_2[22,25] (as verified in Supplementary Movie 1), which can significantly suppress film ablation. Furthermore, the dielectric function of the GST can also be reversibly modulated—that is, without undergoing permanent phase transformation—by employing low-power femtosecond laser pulses[27,28]. This drastically reduces thermal stresses and thus efficiently avoids potential film damage. Hence, future works combining femtosecond laser excitation with the concept presented here could enable the realization of ultrafast SPhP optical devices such as switches and modulators.

Outlook

We also emphasize that the approach presented can be improved further to become even more viable and scalable. As shown in ref. 22, it is technically possible to create or switch multiple resonators at the same time (that is, in a parallel fashion) by using structured illumination or pattern generators in combination with more powerful lasers. We also propose to use a s-SNOM tip to switch nanoscale PCM structures (sketch in Supplementary Fig. 15a). Owing to the optical-antenna effect[1,4], the sharp metallic tip can focus the diffraction-limited illumination into a nanoscale volume at the tip apex and create differently shaped, subwavelength-sized nanostructures (Supplementary Fig. 15b). An extension of the concept presented here could also enable continuous resonance tuning by carefully adjusting the temperature and time during switching (or the laser power levels and time), as shown already for metal–PCM structures[38].

To conclude, we have shown that an ultrathin PCM layer enables all-optical, non-volatile, reversible switching of SPhPs as well as the extreme field confinement that is associated with the ultrashort polariton wavelengths. Our proof-of-concept results only partly reveal the great potential of the PCM–SPhP combination, as both material classes can be optimized. All the results obtained for SPhPs on quartz can be generalized to other polariton systems—for example, SPhPs on other, even 'better' polar crystals[5] (such as SiC, GaN or hBN) or SPPs on noble metals, graphene[16,17,36] and doped semiconductors[39]. The large family of PCMs[40,41] also offers excellent opportunities for various switching functionalities, such as bidirectional (red and blue) frequency shifts[23], metal–insulator transitions[42,43], and ultrafast femtosecond laser modulation. All these exceptional properties could further improve our concept towards future real applications, such as super-resolution imaging in the form of a wavelength-switchable SiC/PCM superlens (Supplementary Fig. 15c), active polariton optics[44,45] for tunable focusing and waveguiding[6,11,12], or reconfigurable metamaterials[46,47] and metasurfaces[48].

Methods

Methods and any associated references are available in the online version of the paper.

Received 11 October 2015; accepted 27 April 2016; published online 23 May 2016

References

1. Hillenbrand, R., Taubner, T. & Keilmann, F. Phonon-enhanced light–matter interaction at the nanometre scale. *Nature* **418,** 159–162 (2002).

2. Dai, S. *et al*. Tunable phonon polaritons in atomically thin van der Waals crystals of boron nitride. *Science* **343,** 1125–1129 (2014).
3. Jacob, Z. Nanophotonics: hyperbolic phonon–polaritons. *Nature Mater.* **13,** 1081–1083 (2014).
4. Hillenbrand, R. Towards phonon photonics: scattering-type near-field optical microscopy reveals phonon-enhanced near-field interaction. *Ultramicroscopy* **100,** 421–427 (2004).
5. Caldwell, J. D. *et al*. Low-loss, infrared and terahertz nanophotonics using surface phonon polaritons. *Nanophotonics* **4,** 44–68 (2015).
6. Huber, A., Ocelic, N., Kazantsev, D. & Hillenbrand, R. Near-field imaging of mid-infrared surface phonon polariton propagation. *Appl. Phys. Lett.* **87,** 081103 (2005).
7. Caldwell, J. D. *et al*. Low-loss, extreme sub-diffraction photon confinement via silicon carbide surface phonon polariton nanopillar resonators. *Nano Lett.* **13,** 3690–3697 (2013).
8. Wang, T., Li, P., Hauer, B., Chigrin, D. N. & Taubner, T. Optical properties of single infrared resonant circular microcavities for surface phonon polaritons. *Nano Lett.* **13,** 5051–5055 (2013).
9. Caldwell, J. D. *et al*. Sub-diffraction, volume-confined polaritons in the natural hyperbolic material: hexagonal boron nitride. *Nature Commun.* **5,** 5221 (2014).
10. Taubner, T., Korobkin, D., Urzhumov, Y., Shvets, G. & Hillenbrand, R. Near-field microscopy through a SiC superlens. *Science* **313,** 1595 (2006).
11. Dai, S. *et al*. Subdiffractional focusing and guiding of polaritonic rays in a natural hyperbolic material. *Nature Commun.* **6,** 6963 (2015).
12. Li, P. *et al*. Hyperbolic phonon–polaritons in boron nitride for near-field optical imaging. *Nature Commun.* **6,** 7507 (2015).
13. Greffet, J. J. *et al*. Coherent emission of light by thermal sources. *Nature* **416,** 61–64 (2002).
14. Xu, X. G. *et al*. One-dimensional surface phonon polaritons in boron nitride nanotubes. *Nature Commun.* **5,** 4782 (2014).
15. Brar, V. W. *et al*. Highly confined tunable mid-infrared plasmonics in graphene nanoresonators. *Nano Lett.* **13,** 2541–2547 (2013).
16. Dai, S. *et al*. Graphene on hexagonal boron nitride as a tunable hyperbolic metamaterial. *Nature Nanotech.* **10,** 682–686 (2015).
17. Woessner, A. *et al*. Highly confined low-loss plasmons in graphene–boron nitride heterostructures. *Nature Mater.* **14,** 421–425 (2015).
18. Caldwell, J. D. *et al*. Atomic-scale photonic hybrids for mid-infrared and terahertz nanophotonics. *Nature Nanotech.* **11,** 9–15 (2016).
19. Spann, B. T. *et al*. Photoinduced tunability of the reststrahlen band in 4*H*-SiC. *Phys. Rev. B* **93,** 085205 (2016).
20. Wuttig, M. & Yamada, N. Phase-change materials for rewriteable data storage. *Nature Mater.* **6,** 824–832 (2007).
21. Bruns, G. *et al*. Nanosecond switching in GeTe phase change memory cells. *Appl. Phys. Lett.* **95,** 043108 (2009).
22. Wang, Q. *et al*. Optically reconfigurable metasurfaces and photonic devices based on phase change materials. *Nature Photon.* **10,** 60–65 (2016).
23. Michel, A. K. U. *et al*. Using low-loss phase-change materials for mid-infrared antenna resonance tuning. *Nano Lett.* **13,** 3470–3475 (2013).
24. Michel, A. K. U. *et al*. Reversible optical switching of infrared antenna resonances with ultrathin phase-change layers using femtosecond laser pulses. *ACS Photon.* **1,** 833–839 (2014).
25. Gholipour, B., Zhang, J., MacDonald, K. F., Hewak, D. W. & Zheludev, N. I. An all-optical, non-volatile, bidirectional, phase-change meta-switch. *Adv. Mater.* **25,** 3050–3054 (2013).
26. Yin, X. *et al*. Active chiral plasmonics. *Nano Lett.* **15,** 4255–4260 (2015).
27. Rudé, M. *et al*. Ultrafast broadband tuning of resonant optical nanostructures using phase change materials. Preprint at http://arXiv.org/abs/1506.03739 (2015).
28. Waldecker, L. *et al*. Time-domain separation of optical properties from structural transitions in resonantly bonded materials. *Nature Mater.* **14,** 991–995 (2015).
29. Karalis, A., Lidorikis, E., Ibanescu, M., Joannopoulos, J. D. & Soljačić, M. Surface-plasmon-assisted guiding of broadband slow and subwavelength light in air. *Phys. Rev. Lett.* **95,** 063901 (2005).
30. Stockman, M. I. Slow propagation, anomalous absorption, and total external reflection of surface plasmon polaritons in nanolayer systems. *Nano Lett.* **6,** 2604–2608 (2006).
31. Zentgraf, T., Liu, Y., Mikkelsen, M. H., Valentine, J. & Zhang, X. Plasmonic luneburg and eaton lenses. *Nature Nanotech.* **6,** 151–155 (2009).
32. Amarie, S. & Keilmann, F. Broadband-infrared assessment of phonon resonance in scattering-type near-field microscopy. *Phys. Rev. B* **83,** 045404 (2011).
33. Njoroge, W. K., Wöltgens, H.-W. & Wuttig, M. Density changes upon crystallization of $Ge_2Sb_{2.04}Te_{4.74}$ films. *J. Vac. Sci. Technol. A* **20,** 230–233 (2002).
34. Dionne, J. A., Sweatlock, L. A., Atwater, H. A. & Polman, A. Planar metal plasmon waveguides: frequency-dependent dispersion, propagation, localization, and loss beyond the free electron model. *Phys. Rev. B* **72,** 075405 (2005).
35. Chakrabarty, A., Wang, F., Minkowski, F., Sun, K. & Wei, Q. H. Cavity modes and their excitations in elliptical plasmonic patch nanoantennas. *Opt. Express* **20,** 11615–11624 (2012).
36. Rodrigo, D. *et al*. Mid-infrared plasmonic biosensing with graphene. *Science* **349,** 165–168 (2015).
37. Brown, L. V. *et al*. Fan-shaped gold nanoantennas above reflective substrates for surface-enhanced infrared absorption (SEIRA). *Nano Lett.* **15,** 1272–1280 (2015).
38. Chen, Y. G. *et al*. Hybrid phase-change plasmonic crystals for active tuning of lattice resonances. *Opt. Express* **21,** 13691–13698 (2013).
39. Law, S., Adams, D. C., Taylor, A. M. & Wasserman, D. Mid-infrared designer metals. *Opt. Express* **20,** 12155–12165 (2012).
40. Lencer, D. *et al*. A map for phase-change materials. *Nature Mater.* **7,** 972–977 (2008).
41. Shportko, K. *et al*. Resonant bonding in crystalline phase change materials. *Nature Mater.* **7,** 653–658 (2008).
42. Zhang, W. *et al*. Role of vacancies in metal–insulator transitions of crystalline phase-change materials. *Nature Mater.* **11,** 952–956 (2012).
43. Siegrist, T. *et al*. Disorder-induced localization in crystalline phase-change materials. *Nature Mater.* **10,** 202–208 (2011).
44. Schwartz, T., Hutchison, J. A., Genet, C. & Ebbesen, T. W. Reversible switching of ultrastrong light-molecule coupling. *Phys. Rev. Lett.* **106,** 196405 (2011).
45. Günter, G. *et al*. Sub-cycle switch-on of ultrastrong light–matter interaction. *Nature* **458,** 178–181 (2009).
46. Driscoll, T. *et al*. Memory metamaterials. *Science* **325,** 1518–1521 (2009).
47. Della Giovampaola, C. & Engheta, N. Digital metamaterials. *Nature Mater.* **13,** 1115–1121 (2014).
48. Yu, N. & Capasso, F. Flat optics with designer metasurfaces. *Nature Mater.* **13,** 139–150 (2014).

Acknowledgements

We thank P. Lingnau for GST film sputtering. This work was supported by the Excellence Initiative of the German Federal and State governments, the Ministry of Innovation of North Rhine-Westphalia, and the DFG under SFB 917 (Nanoswitches).

Author contributions

P.L. and T.T. conceived the concept. P.L. performed the s-SNOM measurements and the theoretical calculations. X.Y. carried out the optical switching and the FTIR experiments. T.W.W.M. performed the simulation. J.H., M.L. and A.-K.U.M. contributed to the optical switching. M.W. and T.T. supervised the project. All the authors discussed the results. P.L., M.W. and T.T. wrote the manuscript.

Additional information

Supplementary information is available in the online version of the paper. Reprints and permissions information is available online at www.nature.com/reprints. Correspondence and requests for materials should be addressed to T.T.

Competing financial interests

The authors declare no competing financial interests.

Methods

The GST ($Ge_3Sb_2Te_6$) films were direct-current magnetron sputter-deposited on 0.5-mm quartz substrates (at a background pressure of 2×10^{-6} mbar, 20 s.c.c.m. Ar flow, deposition rates 0.2 nm s^{-1}) using stoichiometric targets. The as-deposited GST films were in the amorphous state, which was used for the experiments shown in Fig. 2. The GST films used in Figs 3 and 4 were transformed from the as-deposited amorphous to the crystalline state by heating in an oven at 180 °C for 30 min. The laser switching process was then conducted in an in-house-built set-up by focusing a laser beam through a ×10 objective (NA = 0.5) on the sample surface. A nanosecond laser diode source with a central wavelength of 660 nm provides single pulses with tunable output power (up to 400 mW) and pulse duration (from 1 ns to 10 µs). To realize an amorphization process, we used single 15 ns laser pulses with a power of 310 mW. To achieve the crystallization process, a longer (45 ns), lower-power (100 mW) laser pulse was used. An x–y movable sample stage with a maximum range of 4 mm (for each direction) and minimal step size of 1 µm was used to prepare the structures shown in Figs 2–4.

Our s-SNOM system (Neaspec GmbH) is based on a tapping-mode AFM[1]. The metallized AFM tip (radius ~25 nm) vibrates with an amplitude of approximately 50 nm at a tapping frequency $\Omega \approx 270$ kHz. This oscillating tip is illuminated by light from tunable mid-infrared quantum cascade lasers (ranging from 1,050 to 1,184 cm^{-1}, from Daylight Solutions) or a CO_2 gas laser (ranging from 909 to 1,080 cm^{-1}, from Edinburgh Instruments), and the backscattered light from the tip is collected. To suppress background scattering, the detector signals are demodulated at a higher harmonic $n\Omega$ ($n \geq 2$). By means of interferometric detection, the near-field optical amplitude s_n and phase φ_n are obtained (in our case $n = 3$). The optical amplitude signals are shown in our near-field images (Figs 2 and 3).

The far-field reflection spectra were measured with a commercial Bruker-Vertex-70 Fourier transform infrared (FTIR) spectrometer in combination with a Hyperion-2000 infrared microscope. This combination, together with a knife-edge aperture (about 20×20 μm^2) allows the recording of micro-FTIR reflection spectra. The objective used has a ×36 magnification (NA = 0.5) with an incident angular range from 10° to 30°. A mercury cadmium telluride (MCT) detector with a tunable polarizer was used to record the polarized FTIR spectra in Fig. 4. The FTIR spectra measured from the investigated phase-change structures were normalized to a background spectrum measured with the same aperture on the surrounding flat GST film. Therefore, the spectra shown in Fig. 4 show the relative reflectivity. The signal-to-noise ratio of the spectra was defined by 400 scans with a pixel size of 2 cm^{-1}.